Chemical Engineering Journal 519 (2025) 165272

Contents lists available at ScienceDirect

Chemical Engineering Journal

journal homepage: www.elsevier.com/locate/cej

High-current-density electrosynthesis of formate from captured CO_2 solution by MOF-derived bismuth nanosheets

Tianlei Li [a], Nabin Subedi [b], Sujin Kang [a], Qiqi Mao [a], Yuhuan Fei [a], Shuang Gu [b,*], Wenzhen Li [a,**]

[a] Department of Chemical and Biological Engineering, Iowa State University, Ames, IA 50011, USA
[b] Department of Mechanical Engineering, Wichita State University, Wichita, KS 67260, USA

A B S T R A C T

Greenhouse gas emissions present a significant challenge to humanity, and utilizing renewable electricity to convert emitted CO_2 into value-added products offers a promising solution; however, traditional CO_2 capture and regeneration processes remain energy-intensive, restricting the overall system efficiency and decarbonization efficacy. In this study, an advanced direct reduction of captured CO_2 with large current densities for formate electrosynthesis was demonstrated without the need for CO_2 regeneration or compression. The bismuth nanosheet (DRM-BiNS) was synthesized by direct reduction of a Bi-based MOF, representing a new class of catalytic materials with a large surface area and interconnected pores, suitable for the direct reduction of captured CO_2. By seamlessly combining experimentation and simulation, insights into the structure-parameter-performance relation were acquired in a flow cell setting, including critical membrane-electrode distance, cell orientation, and pumping flow rate. Important flow-cell components, such as catholyte volume, electrode substrate, membrane choice, and ionomer type, were also carefully examined to enhance the cell performance. In sharp contrast to prior studies limited to current densities below 20 mA/cm^2 in bicarbonate-based captured CO_2 solutions, this work demonstrates a remarkable current density of 300 mA/cm^2 with an FE to formate comparable to the case with gas-fed CO_2 reduction. Moreover, the process sustained an FE above 50% at a high current density of 500 mA/cm^2. The DRM-BiNS catalyst exhibited outstanding selectivity, activity, and stability, significantly outperforming oxide-derived bismuth nanosheets (OD-BiNS) in captured CO_2 reduction. These findings offer critical insights into the development of sustainable and scalable CO_2 utilization technologies.

1. Introduction

To address the critical challenges posed by greenhouse gas emissions and the excessive consumption of fossil fuels [1], leveraging renewable electricity to convert emitted CO_2 into value-added products offers a promising solution [2–4]. Depending on the catalyst materials and reaction conditions, the CO_2 reduction products range from C_1 compounds (e.g., carbon monoxide, methane, and formate/formic acid) [5–7] to C_2 (e.g., ethylene, ethanol) [8–10] and even C_{2+} products (e.g., propanol) [11]. Among these products, formate/formic acid holds significant industrial potential due to its high faradaic efficiency (FE > 80%) and diverse applications [12]. For instance, formate can serve as an eco-friendly deicing agent [13], a fuel for direct fuel cells (formic acid) [14], or as a precursor for upgrading to more valuable chemicals like formamide [15]. Compared to gaseous products, formate is technically and economically advantageous in terms of collection, storage, and transportation [16].

Several materials, including tin (Sn), indium (In), antimony (Sb), and bismuth (Bi), have been identified as effective catalysts for converting CO_2 to formate [17–20]. For example, Zhang et al. reported a tin nanocrystal catalyst achieving >93% FE to formate at a current density exceeding 10 mA/cm^2 [17], while Ma et al. demonstrated a sulfur-doped indium catalyst with over 85% FE to formate across a current density range of 25–100 mA/cm^2 [19]. Among these materials, bismuth has garnered significant attention due to its earth abundance, low cost, low toxicity, high tolerance to the competing hydrogen evolution reaction (HER), and favorable binding energy for the formate intermediate (*OCHO) [21–24]. Recent studies have explored various bismuth-based catalysts, including nanosheets, nanotubes, and bi-metallic catalysts, highlighting their high activity and selectivity for CO_2-to-formate reduction reactions [25–27]. Han et al. synthesized ultrathin bismuth nanosheet (BiNS) via in situ transformation of layered bismuth oxyiodide (BiOI) nanosheet template. The obtained 2D material with enlarged surface area and enriched active sites showed excellent selectivity (~95% FE to formate) but suffered relatively low activity (a current density of 16 mA/cm^2) [25]. In contrast, Liu et al. developed a

* Corresponding author.
** Correspondence to: W. Li, Chemical and Biological Engineering, Biorenewables Research Laboratory, Iowa State University, Ames, IA 50011, USA.
E-mail addresses: shuang.gu@wichita.edu (S. Gu), wzli@iastate.edu (W. Li).

https://doi.org/10.1016/j.cej.2025.165272
Received 13 March 2025; Received in revised form 4 June 2025; Accepted 22 June 2025
Available online 1 July 2025

bismuth-based metal-organic framework (MOF) that achieved both extraordinary selectivity (93% FE to formate) and activity (current density of 150 mA/cm^2 with gas-fed CO_2), outperforming most previously reported bismuth-based catalysts [28]. Notably, the Bi-based MOF provides a large surface area, rich interconnected pores, and abundant Bi sites, which spontaneously transform into electrocatalytically active thin sheets during the CO_2 Reduction reaction (CO2RR).

Industrial-scale reaction rates (e.g., >200 mA/cm^2) have been demonstrated in flow cells using high-purity gas-fed CO_2 as a feedstock. However, the capture and regeneration of high-purity CO_2 are deemed energy-intensive, consequently complicating the overall decarbonization effort [29–31]. This challenge has motivated the use of bicarbonate as an alternative feedstock, bypassing the energy-demanding CO_2 capture and regeneration steps. For instance, Zhang et al. achieved a 95.5% FE to formate at a current density of 11.2 mA/cm^2 using a Bi-based MOF in the aqueous phase [32]. Despite its promise, this approach faces limitations due to the low solubility and diffusivity of CO_2 in aqueous solutions [33]. By employing cation exchange membranes or bipolar membranes, protons from the membrane react with bicarbonate to in-situ generate CO_2 (*i*-CO_2), which is subsequently reduced by the cathode catalyst. For example, Lee et al. reported a silver-based catalyst capable of reducing CO_2 to CO in bicarbonate solutions with an FE of 82% at 100 mA/cm^2, comparable to gas-phase CO_2 reduction performance [34]. Several studies have employed Bi-based MOFs and aqueous feedstocks for formate production. However, the current density is far below the industrial needs. In addition, the structure-performance relationship, microenvironment, and key parameters of the CO_2 flow cell have not been fully investigated, certainly not through a combined study between experimentation and simulation using powerful software such as COMSOL Multiphysics.

In this study, we report a bismuth nanosheet made by in situ reduced Bi-based MOF for CO_2 reduction in the aqueous phase at high current densities. By engineering the cell configuration, we achieved a formate-oriented FE comparable to gas-fed CO_2 reduction at current densities up to 300 mA/cm^2. Compared to the previously published oxide-derived bismuth nanosheets (OD-BiNS) study from our group [35], which has demonstrated outstanding CO_2 reduction to formate activity and stability, the MOF-derived material demonstrated exceptional CO_2 utilization in the aqueous phase. In particular, we achieved an FE of 82% to formate at 200 mA/cm^2 and doubled FEs to formate at 400 and 500 mA/cm^2 as compared with OD-BiNS.

2. Experimental and simulation methods

2.1. Chemicals and materials

All materials and chemicals were used as received without further purification. Platinum foil (99.99%) was purchased from Strem Chemicals Inc. Bismuth nanoparticles (99.9% purity and 80 nm of average particle size) were acquired from US Research Nanomaterials Inc. Bismuth(III) nitrate pentahydrate [$Bi(NO_3)_3{\cdot}5H_2O$, 98%], 1,3,5-benzenetricarboxylic acid (H_3BTC, 95%), potassium bicarbonate ($KHCO_3$, 99.7%), *N*, *N*-dimethylformamide (DMF, 99.5%) were purchased from Sigma-Aldrich. Nafion ionomer (5%) suspension solution was purchased from Ion-Power. Inc. Sustainion ionomer (5%) suspension solution was purchased from Dioxide Materials. Nafion 115 cation-exchange membrane (CEM), Fumasep FBM bipolar membrane (BPM), nickel foam, iridium oxide (IrO_2) catalyst powder, and all carbon paper substrates were purchased from the Fuel Cell Store. Carbon dioxide (CO_2) gas, at research grade (99.999%), was purchased from Airgas, Inc.

2.2. Bismuth MOF synthesis and catalyst preparation

Bismuth-based and 1,3,5-benzenetricarboxylic acid-derived MOF (Bi-BTC) was synthesized from $Bi(NO_3)_3$ and H_3BTC via a hydrothermal method. Specifically, 0.3 g of $Bi(NO_3)_3{\cdot}5H_2O$ and 1.5 g of H_3BTC were dissolved in a solvent mixture of 24 mL methanol and 96 mL DMF. After stirring for 15 min, the clear solution was transferred into a 150 mL Teflon-lined stainless-steel autoclave, followed by heating at 120 °C for 24 h in a muffle furnace. After the hydrothermal reaction, Bi-BTC, as the resulting white precipitate, was obtained and collected by centrifugation, first washed with methanol three times, and then dried overnight in a vacuum oven at 60 °C.

To prepare a CO_2 reduction-active catalyst, the as-synthesized Bi-BTC was sprayed onto carbon paper and subjected to cyclic voltammetry (CV) reduction. The spray ink was prepared by mixing 10 mg of Bi-BTC synthesized above, 50 mg of 5% ionomer solution (for 20 wt% ionomer content), and 3 mL of isopropanol. After spraying the ink onto a carbon paper, the as-obtained electrode underwent CV reduction in a CO_2-saturated 0.5 M $KHCO_3$ solution, cycling between −1.0 V and −1.6 V vs. Ag/AgCl for 20 cycles at a scan rate of 50 mV/s. The reduced catalyst was designated as Directly-Reduced MOF Bismuth Nanosheet (DRM-BiNS).

2.3. Catalyst preparation for control experiments

As a control, the Bi_2O_3 oxide-derived Bi nanosheet (OD-BiNS) catalyst was prepared precisely following the method previously reported by our group. In brief, 0.89 g of $Bi(NO_3)_3{\cdot}5H_2O$ was dissolved in 30 mL of deionized water, and then the pH was adjusted to 12 using a 1 M KOH solution. The mixture was stirred for 2 h, and the white precipitated Bi_2O_3 was obtained and collected by centrifugation, followed by drying overnight in a vacuum oven at 60 °C. It was converted to CO2RR active catalyst through the same electro-reduction method as the DRM-BiNS, and it was named oxide-derived bismuth nanosheet (OD-BiNS).

2.4. Characterization methods

Scanning electron microscopy (SEM) images and energy dispersive spectroscopy (EDS) data were collected using an FEI Quanta 250 FE-SEM. X-ray diffraction (XRD) was performed on a Rigaku SmartLab diffractometer with Copper K-α radiation ($\lambda = 0.15418$ nm) operating at 40 kV and 44 mA. Transmission electron microscopy (TEM) images and EDS spectra were obtained using a JEOL 200 kV JSM-2100 scanning transmission electron microscope equipped with a Gatan OneView 4 K camera. Formate was quantified by Thermo Scientific Dionex Easion ion chromatography (IC), and the gas product was quantified by Agilent 8890 gas chromatography (GC) system.

2.5. Electrochemical measurements

Electrochemical measurements were carried out using a BioLogic SP-150 electrochemical workstation. For H-type cell tests, the two compartments were separated by a Nafion 115 membrane and CO_2-saturated 0.5 M $KHCO_3$ was used as the electrolyte. The catalyst was sprayed onto 1 cm × 1 cm Freudenberg H23 carbon paper, with catalyst loading normalized to 1 mg-Bi/cm^2, where Bi content was measured by thermogravimetric analysis (TGA), results summarized in Table S1. CV measurements were conducted by scanning between −1.0 V and −1.6 V vs. Ag/AgCl at a scan rate of 10 mV/s. The electrochemical impedance spectroscopy (EIS) data were collected at −1.3 V vs. Ag/AgCl. Area-specific capacitance was measured by scanning from −0.8 V to −1.0 V vs. Ag/AgCl at various scan rates.

The conversion of potential between the saturated Ag/AgCl reference electrode and Reversible Hydrogen Electrode (RHE) is calculated by:

$$E(\text{V vs.RHE}) = E(\text{V vs.Ag/AgCl}) + 0.197 + 0.059 \times \text{pH}$$

The pH of 7.5 reported in this study was measured by a pH meter for CO_2-saturated 0.5 M $KHCO_3$ solution.

In flow cell tests, the electrodes were separated using either a cation-exchange membrane or a bipolar membrane. For CEM-based cells, the

anode comprised 2 cm × 2 cm carbon cloth loaded with 0.5 mg-IrO_2/cm^2, and 0.1 M H_2SO_4 was used as the anolyte. For BPM-based cells, the anode was simply a 2 cm × 2 cm nickel foam, and 1 M KOH was used as the anolyte. The cathode was prepared by spraying catalysts, normalized to 0.5 mg-Bi/cm^2, onto a 2 cm × 2 cm carbon paper substrate. CO_2 was supplied to saturate 2.5 M $KHCO_3$ to serve as the catholyte that mimicked the captured CO_2 solution and was referred to as "captured CO_2 solution", and a peristaltic pump was used to circulate the electrolyte through the flow cell. For convenient discussion, the pumping flow rate measured in revolutions per minute (rpm) was reported in this work, which can be converted to milliliters per minute (mL/min) by multiplying by a conversion factor of 0.87. As a comparison to the "captured CO_2" solution-fed flow cell, a well-established catholyte-free flow cell whose cathode was fed with high-purity CO_2 gas was also evaluated for CO2RR and referred to as "gas-fed CO_2 flow cell. In the gas-fed CO_2 flow cell, the cathode was prepared by spraying DRM-BiNS catalyst ink onto a gas diffusion layer (GDL) (Sigracet 39 BB) with a consistent catalyst loading of 0.5 mg/cm^2. CO_2 gas is purged to the cathode chamber at 15 sccm. The anolyte, 1 M KOH, was circulated via a peristaltic pump, with a nickel foam as anode separated from the cathode by an anion exchange membrane (AEM) (Sustainion X37-50 Grade RT).

Formate was quantified using IC calibrated in the range of 0–1 mM. Product solutions were diluted with deionized water to fall within this concentration range. FE was calculated using the formula:

$$FE = \frac{n \bullet c \bullet V \bullet F}{Q}$$

where n is the number of charges transferred in this reaction ($n = 2$ for formate), c is the formate concentration detected from IC (mol/L), V is the catholyte volume (L), F is the Faraday constant (96,485C/mol), and Q is the total charge applied to the cathode during entire cell operation (C). Unless stated otherwise, FE was measured over a consistent interval of 30-minute operation immediately following a 15-minute pre-run for all experiments, except for the durability test. Unless indicated otherwise, the experiment conditions were, using 30 mL of catholyte volume, 30 rpm of flow rate, 300 μm gasket thickness to control the exact membrane-cathode distance, 2.5 M $KHCO_3$ as catholyte, 0.5 mg-Bi/cm^2 of catalyst loading, H23 carbon paper as cathode substrate, and Sustainion as ionomer with 20% of ionomer content.

2.6. COMSOL simulation

The 2D concentration profiles of relevant species inside the catholyte with specified cell condition (both orientation and thickness) at a given set of operational conditions (both applied current density and flow rate) were computed by the COMSOL Multiphysics software (Ver. 6.3). The 2D concentration profiles of relevant species inside the catholyte with specified cell conditions (both orientation and thickness) at a given set of operational conditions (both applied current density and flow rate) were computed by the COMSOL Multiphysics software (Ver. 6.3). The general simulation conditions are restricted as follows. The catholyte has four designated boundaries. The 1st is an ion-exchange membrane (either CEM or BMP) that provides H^+ flux equivalent to the applied current density. The 2nd is the cathode surface that provides OH^- flux equivalent to half of H^+ flux (based on $CO_2 + H_2O + 2e^- = HCOO^- + OH^-$). For simplicity, $HCOO^-$ flux from the cathode surface is not included, because of the OH^- dominance over $HCOO^-$ (more than tripled diffusion coefficient). The 3rd and 4th are the inlet and outlet of the catholyte, respectively. The fluid velocity is directly proportional to the peristaltic flow rate (10–50 rpm) and inversely proportional to the channel thickness of the catholyte. Ionic diffusion coefficient: $D(H^+)$, $D(K^+)$, $D(OH^-)$, $D(HCOO^-)$, $D(HCO_3^-)$, $D(CO_3^{2-})$, $D(H_2CO_3)$, and $D(CO_2)$ = 9.312, 1.957, 5.26, 1.50, 1.105, 2.0, 2.0, and 1.96 × 10^{-9} m^2/s, respectively. Unless otherwise specified, Gibbs free energy data and diffusion coefficient data were taken from the Lange's Handbook of Chemistry (15th Ed) and the CRC Handbook of Chemistry and Physics (95th Ed), respectively.

The detailed simulation method can be found in SI.

3. Results and discussion

3.1. Materials synthesis and catalyst characterization

The overarching synthesis procedure for Directly Reduced MOF-derived Bismuth Nanosheet (DRM-BiNS) is presented in Fig. 1. Succinctly, the Bi-BTC MOF was first synthesized via a modified hydrothermal method [28] and subsequently reduced by direct cyclic voltammetry in a CO_2-saturated 0.5 M $KHCO_3$ solution, resulting in the formation of a nanosheet morphology. Fig. 2a shows the nanorod structure for the as-synthesized Bi-BTC MOF. After the electrochemical reduction, Bi-BTC was transformed into DRM-BiNS that possesses a two-dimensional (2D) nanosheet structure (Fig. 2b), providing a large specific surface area necessary for critical adsorption of reaction intermediates on active sites. As shown in Fig. 2c, the strong presence of metallic Bi in the DRM-BiNS revealed by the X-ray diffraction (XRD) pattern indicates the successful conversion of high valence Bi in the MOF to the metallic Bi during the electroreduction process. The ultrathin 2D nanosheet structure was further visualized in HR-TEM imaging (Fig. 2d). Moreover, as revealed by the HR-TEM image (Fig. 2e), the lattice spacing of 0.328 nm corresponds to the Bi (0 1 2) facet, which matches the metallic Bi structure identified in the XRD results. The associated energy-dispersive X-ray spectroscopy (EDS) elemental mapping of DRM-BiNS shows a high abundance of bismuth but a very low content of oxygen, suggesting the high purity of metallic bismuth. Note that the observed carbon signals are residues from the MOF reduction process, and the copper signals are from the TEM grids.

First, we compared the CO_2 electro-reduction performance of our DRM-BiNS catalysts with the reported OD-BiNS [35] with CO_2-saturated 0.5 M $KHCO_3$ as the feedstock (or "captured CO_2 solution" for simplicity). We chose OD-BiNS as a comparison because both OD-BiNS and DRM-BiNS are nanosheets, enabling a meaningful comparison that underscores the superior performance of DRM-BiNS in CO_2-limited conditions (2.5 M $KHCO_3$ solution or in H-type cell test). As shown in Fig. 3a, DRM-BiNS exhibits substantially superior CO2RR activity to OD-BiNS in the CV study obtained in an H-type cell. The forward CO2RR current under −0.9 V vs. RHE is −48.45 mA for DRM-BiNS, which is 82% larger than that of OD-BiNS with the same Bi loading (−26.64 mA), or 6.67 times larger than commercial Bi (−7.26 mA). The improved activity for DRM-BiNS can be attributed to its large surface area and extensive porous structure, which not only provides more active sites for reaction but also grants improved accessibility to dissolved CO_2. As shown in Fig. S1, the 2D nanosheet structure of DRM-BiNS possesses a slimmer structure and a more interconnected architecture, exposing more active sites. The EIS study (Fig. 3b) shows that the charge-transfer resistance is much smaller for DRM-BiNS (19 Ω) than for OD-BiNS (29 Ω), consistent with the observed higher CO2RR activity. Specific capacitance tests were performed to further evaluate the electrochemical surface area (ECSA) of the catalyst (Fig. 3c). Although both catalysts exhibit nanosheet morphologies, DRM-BiNS shows approximately 1.6 times the specific capacitance of OD-BiNS (3.8 vs. 2.4 mF/cm^2), in concert with the lowered charge-transfer resistance. Take the example at −0.85 V vs. RHE, the current density for OD-BiNS is approximately 20 mA/cm^2, while for DRM-BiNS it reaches around 36 mA/cm^2. This ratio closely aligns with the specific capacitance ratio, indicating that both catalysts exhibit similar intrinsic activity. The Tafel slope can provide insights into the rate-determining step (RDS) of CO2RR. Tafel analysis revealed similar Tafel slopes: −112 mV/dec for DRM-BiNS and −124 mV/dec for OD-BiNS (Fig. 3d). Both Tafel slopes are very close to the typical Tafel slope of 118 mV/dec, strongly suggesting the first electron transfer step is the RDS, and the equation is:

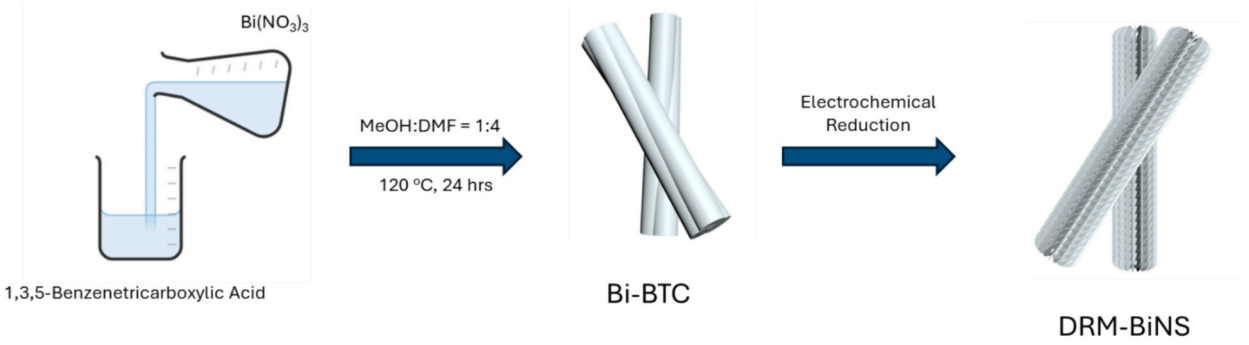

Fig. 1. Schematic illustration of the catalyst synthesis process.

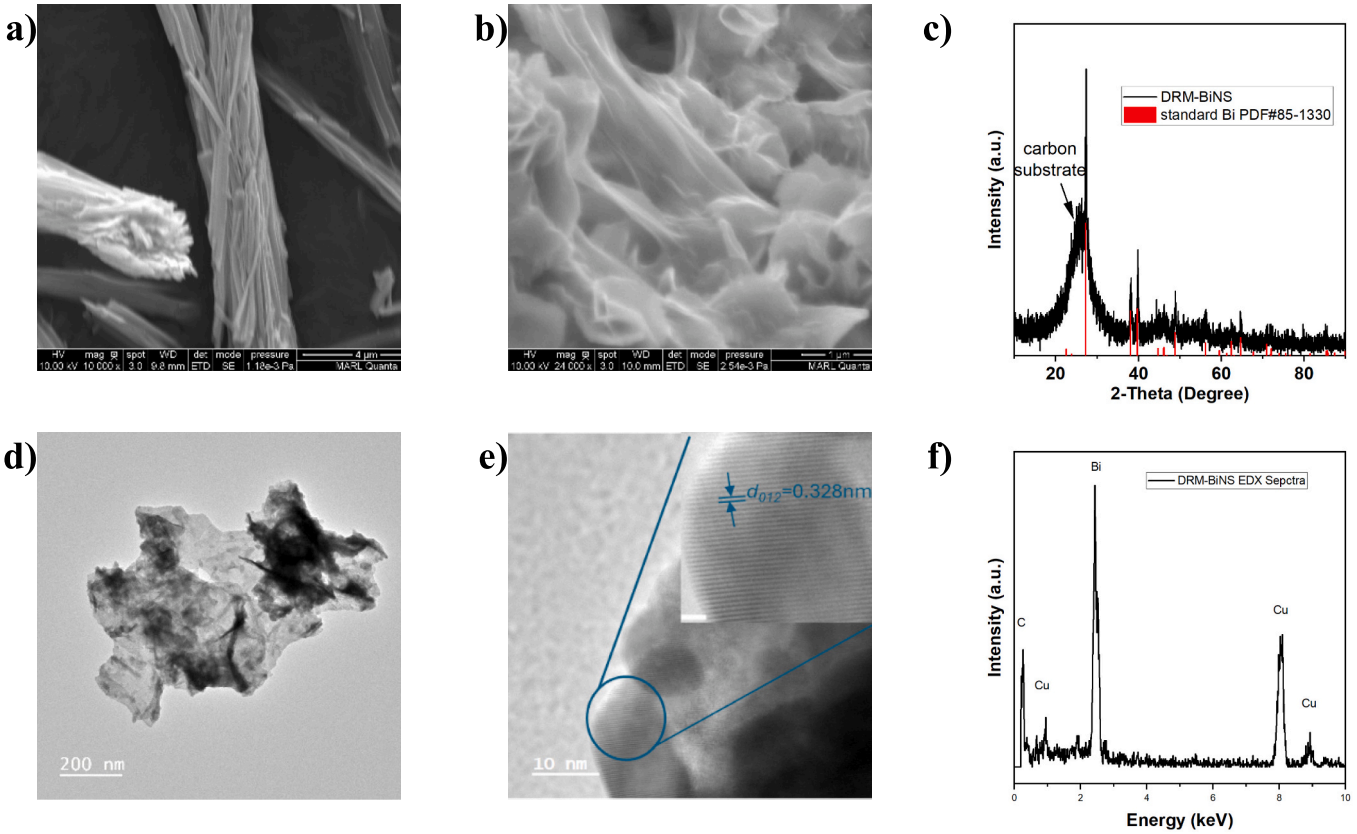

Fig. 2. Characterization of Bi-BTC MOF and reduced DRM-BiNS. (a) SEM image of as-synthesized Bi-BTC MOF. (b) SEM image of DRM-BiNS. (c) XRD spectra of DRM-BiNS and standard metallic bismuth. (d) HR-TEM image of DRM-BiNS with high magnification. (e) HR-TEM image of DRM-BiNS with ultrahigh magnification. (f) TEM-EDX element mapping of DRM-BiNS (Cu signals are from the TEM holder).

$CO_2 + e^- \rightarrow CO_2^{\cdot -}$ [36,37]. These results collectively confirm that the superior activity of DRM-BiNS arises from the availability of substantially more active sites rather than any significant difference in reaction mechanisms.

The electrocatalytic performance of these Bi catalysts was first evaluated using gas-fed CO_2 as the feedstock because gaseous CO_2 electroreduction is generally considered to be less challenging. As shown in Fig. S2, DRM-BiNS demonstrates outstanding activity and high selectivity towards formate production in gas-fed CO_2 reduction. Specifically, DRM-BiNS reached 92% FE to formate at 100 mA/cm^2, and the catalyst maintained around 80% FE to formate at a current density as high as 300 mA/cm^2, highlighting its remarkable capability of active CO_2 reduction to formate.

3.2. *Insights into the structure-parameter-performance relation in the flow cell*

We systematically investigated DRM-Bi-NS for CO2RR from a feedstock of CO_2-captured solution (i.e., CO_2-saturated $KHCO_3$ solution) in a flow cell setting. Fig. 4a presents the schematic of a typical MEA-based flow cell design. Note that there is no CO_2 directly supplied to the flow cell. Fig. 4b illustrates the reaction process and microenvironment at the interface between the membrane and the catalyst layer. In a flow cell, in-situ CO_2, or *i*-CO_2, in the system is locally generated through the reaction between bicarbonate and protons provided by the membrane, making efficient utilization of *i*-CO_2 a critical factor in achieving high FE. Previous work by Lee's group demonstrated that the distance between electrodes is essential for delivering high cell performance [38]. When the electrode is too close to the membrane, a lower pH environment is

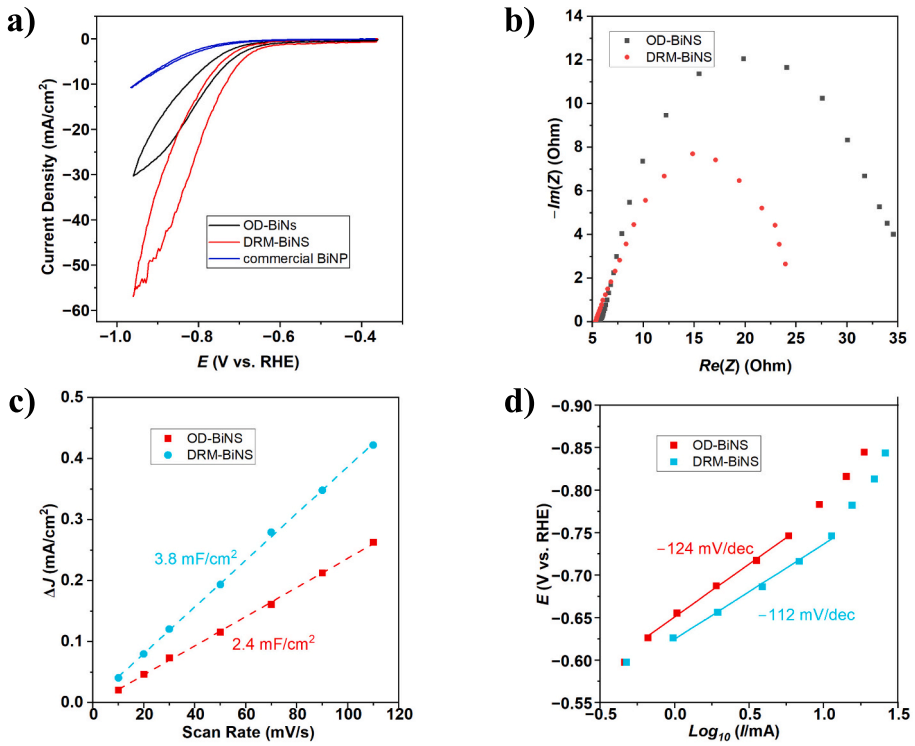

Fig. 3. Electrochemical characterization of DRM-BiNS and OD-BiNS in H-type cell setting. Test conditions: 1 mg-Bi/cm^2 of catalyst loading, CO_2-saturated 0.5 M $KHCO_3$ solution as the electrolyte. (a) CV results of commercial bismuth nanoparticles (BiNP), OD-BiNS, and DRM-BiNS. (b) Nyquist plot from EIS analysis. (c) Specific capacitance measurement. (d) Tafel slope measurement.

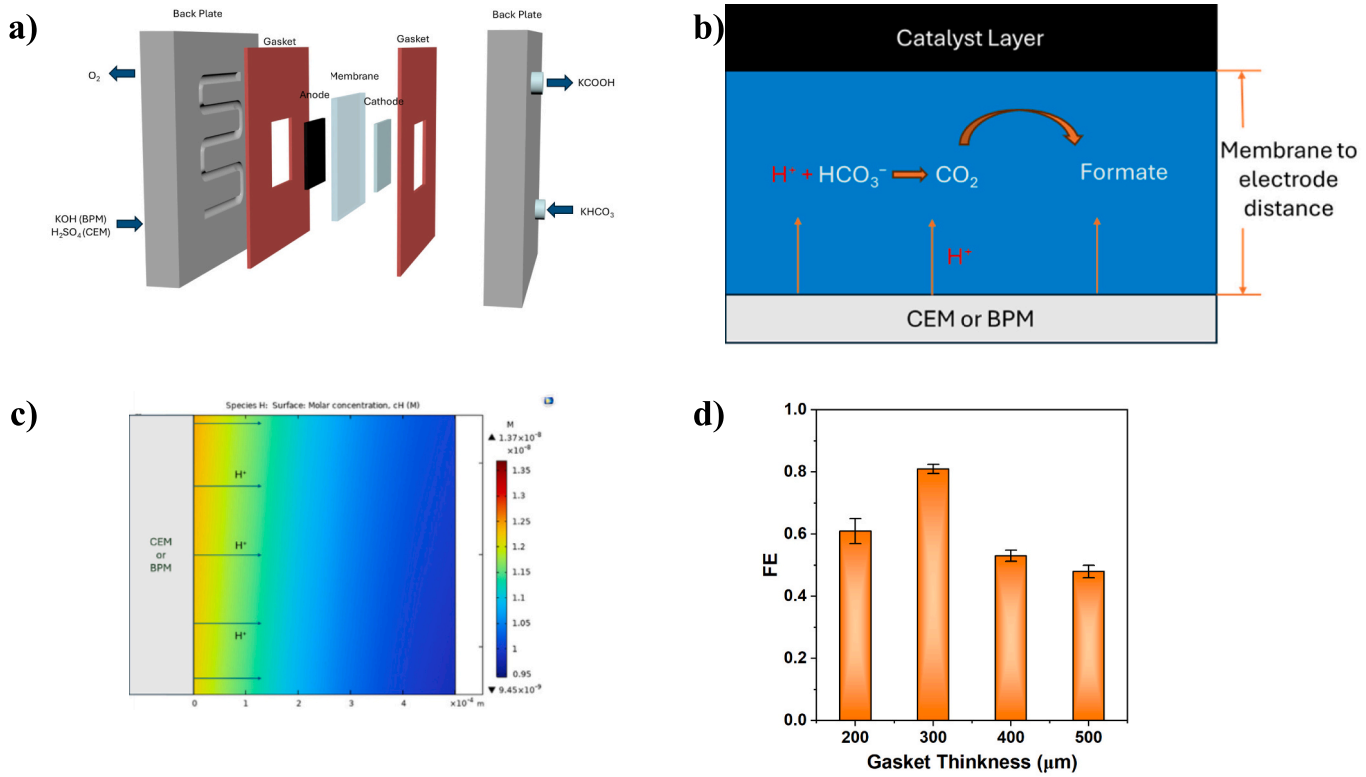

Fig. 4. Flow cell setting and important cathode condition. (a) Typical MEA flow cell configuration. (b) Conceptual illustration of the catholyte reaction environment. (c) A representative COMSOL simulation model and species distribution. (d) The impact of membrane-cathode distance on experimental FE. (Distance was controlled by gasket with a precise thickness ranging from 200 to 500 μm.) Experiment conditions: 30 rpm pump rate, 30 mL catholyte volume, horizontal orientation, 300 μm between membrane and cathode, 0.5 mg-Bi/cm^2 catalyst loading, 20% ionomer content, and H23 carbon paper as the substrate.

created, which promotes the competing hydrogen evolution reaction (HER) as a competing process. Conversely, the electrode is placed too far apart, resulting in a reduced *i*-CO_2 concentration and thus decreased CO2RR performance.

To determine the optimal distance between the membrane and the electrode, COMSOL Multiphysics was employed to simulate the concentration and flux of ion species and CO_2 species (both "aqueous dissolved CO_2", or $CO_{2,aq}$, and "gaseous bubbling CO_2", or $CO_{2,gas}$), as shown in Figs. 4c and S3. We examined the concentration profiles of the three most important aqueous species (H^+, OH^-, and $CO_{2,aq}$) at 5 different channel thicknesses (100, 200, 300, 400, and 500 μm) at the same peristaltic pumping rate (30 rpm) and the same current density (100 mA/cm^2). To match 100 mA/cm^2 of current density, a constant H^+ flux (1.036 μmol cm^{-2} s^{-1}) was incorporated consistently as the boundary condition on the surface of the membrane (CEM or BPM) for all cases. A constant OH^- flux (0.518 μmol cm^{-2} s^{-1}), or half of the H^+ flux, was adopted as the boundary condition on the other side of the catholyte channel mimicking the cathode surface. For simplicity, $HCOO^-$ flux from the cathode surface was not included, because of the OH^- dominance over $HCOO^-$ (more than tripled diffusion coefficient). When increasing the catholyte channel thickness from 100 μm to 500 μm, the maximum OH^- concentration remains flat from 1.01×10^{-6} M to 1.06×10^{-6} M (i.e., 5% increase); but the maximum H^+ concentration rises from 1.21×10^{-8} M to 1.37×10^{-8} M (13% increase); and so does the $CO_{2,aq}$ concentration from 3.37 mM to 3.80 mM (the same 13% increase). Clearly, there is a tradeoff in the catholyte channel thickness: raising H^+ concentration adversely affects the FE towards $HCOO^-$; but increasing $CO_{2,aq}$ concentration directly favors the CO2RR. Specifically, a critical distance of 300 μm divides the catholyte channel in two regions in the middle cell height: the near region (0–300 μm) with drastic increase in H^+ concentration (5%–23%), and the far region (300–500 μm) with mild increase in H^+ concentration (0%–5%). As shown in Fig. 4d, the highest FE (82%) was indeed observed at the cathode-membrane distance of 300 μm on the same DRM-BiNS under the same test conditions (100 mA/cm^2 and 30 rpm) among other distances (such as 200 μm with 61% and 500 μm with 47%), in accordance with simulation results.

A significant challenge in captured CO_2 reduction lies in the slower CO_2 diffusion compared to gas-phase CO_2RR. It was speculated that *i*-CO_2 exists in two phases: aqueous dissolved CO_2 and gaseous CO_2 bubbles. Dissolved CO_2 moves with the electrolyte, while CO_2 bubbles rise upward due to the buoyancy force, as illustrated in the scheme in Fig. S4. To verify the hypothesis, we used COMSOL to simulate the horizontal and vertical orientations of the cell, as shown in Fig. S5. The cell orientation has little effect on the $CO_{2,aq}$ generation: the concentration range of $CO_{2,aq}$ in the cathode electrolyte is very close to the vertical cell orientation (2.65–3.80 mM) and the horizontal cell orientation (2.64–3.75 mM), based on 500 μm of channel thickness and 30 rpm of peristaltic flow rate (2.18 cm/s) at 100 mA/cm^2 of current density. However, the maximum $CO_{2,gas}$ volume fraction of the horizontal cell orientation is more than double that of the vertical cell orientation (15.0% vs. 7.1%). The average $CO_{2,gas}$ volume fraction is also larger for the horizontal cell orientation than for the vertical one (0.33% vs. 0.26%). The density of CO_2 gas is roughly 1/700th of that of the liquid electrolyte (0.00182 kg/L vs. 1.25 kg/L), and thus the gravity makes the horizontal cell orientation retain the $CO_{2,gas}$ inside the catholyte channel longer than the vertical one, resulting in such larger volume fraction at the steady state. The larger $CO_{2,gas}$ volume fraction greatly favors the desirable CO2RR in comparison to the undesirable

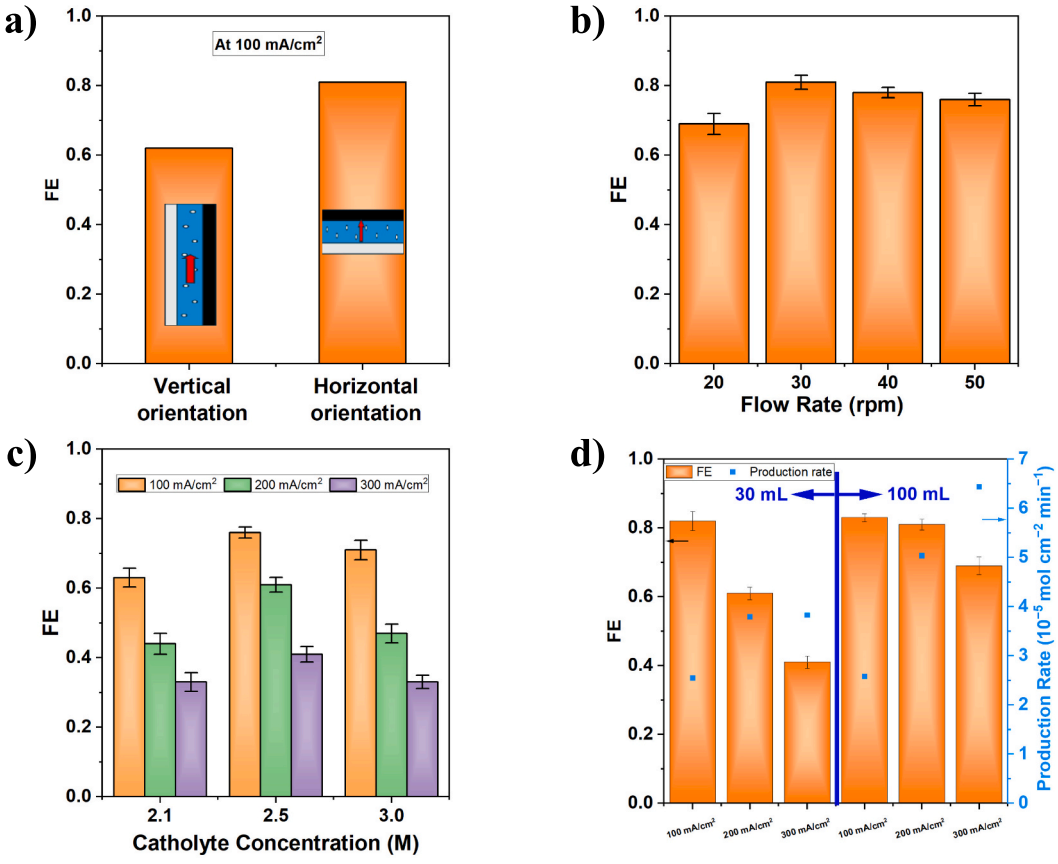

Fig. 5. Impacts of key cell parameters on FE in the flow cell setting. (a) Cell orientation. The schemes of the orientations were embedded, where the grey part represents the membrane; the black part represents the catalyst layer; and the red arrow indicates the CO_2 bubble movement direction. (b) Pumping flow rate. (c) Concentration of $KHCO_3$. (d) Volume of catholyte (2.5 M $KHCO_3$). Experiment conditions: 30 rpm pump rate, 30 mL catholyte volume, horizontal orientation, 300 μm between membrane and cathode, 0.5 mg-Bi/cm^2 catalyst loading, 20% ionomer content, and H23 carbon paper as the substrate.

HER. As shown in Fig. 5a, it is intriguing that the FE is indeed much higher for the horizontal cell orientation than for the vertical cell orientation (81% vs. 62%) under the same test conditions (100 mA/cm^2 and 30 rpm), which underscores the critical importance of accessing *i*-CO_2 for captured CO2RR. This result also implies that *i*-$CO_{2,gas}$ is equally important to *i*-$CO_{2,aq}$ for captured CO_2 reduction. Following the methods described in Lee's work [35], inert porous materials were also examined here to regulate *i*-CO_2. However, those porous materials did not bring noticeably improved results, as shown in Fig. S6. We speculate that the transport of *i*-$CO_{2,aq}$ may be facilitated by the porous filling media through increased local velocity, but the transport of *i*-$CO_{2,gas}$ bubbles (a few tens of microns) is certainly hindered by the smaller pore sizes (typically a few microns) in the filter papers.

The flow rate is another critical factor influencing the regulation of local pH. Insufficient bicarbonate flow cannot effectively neutralize protons, possibly leading to excessively low local pH. However, too high flow rates may flush out *i*-CO_2 of the electrode chamber too soon. To find the optimal flow rate, we used COMSOL to simulate the micro-environment by fixing the catholyte channel thickness of 300 μm and a current density of 100 mA/cm^2, we examined the impact of peristaltic pumping rate (20, 30, 40, and 50 rpm) with their corresponding average fluid velocities (2.42, 3.63, 4.83, and 6.04 cm/s, respectively), as shown in Fig. S7. When the peristaltic pumping rate was raised from 30 rpm to 50 rpm, the maximum H^+ concentration drops from 1.43×10^{-8} M to 1.17×10^{-8} M (or 18% decrease); the maximum $CO_{2,aq}$ concentration follows the same trend: 3.97 mM to 3.27 mM (the same 18% decrease). Meanwhile, the maximum OH^- concentration also remains flat from 1.05×10^{-6} M to 1.02×10^{-6} M (3% decrease). A similar tradeoff in the pumping flow rate is anticipated: lowering H^+ concentration alleviates the HER side reaction; but reducing $CO_{2,aq}$ inevitably weakens CO_2RR. Among the four tested flow rates in Fig. 5b, we observed that the optimal pumping rate is 30 rpm with the highest FE (81%), compared with 20 rpm (69%), 40 rpm (79%), and 50 rpm (77%) under the same test conditions (100 mA/cm^2 and 300 μm). The experimental observation of the optimal pumping rate is in line with simulation results. Furthermore, variations in catholyte concentration are common across studies in the research on the captured CO_2 reduction. Fig. 5c illustrates the effects of different catholyte concentrations. Lower concentrations lead to similar scenarios of a low flow rate, where bicarbonate is insufficient to maintain *i*-CO_2 concentrations. Conversely, excessively high bicarbonate concentration increases carbonate levels. It is possible that increased fluid density and viscosity brought by increasing bicarbonate concentration hinders *i*-CO_2 transport and thereby the CO2RR performance.

3.3. Rationalized engineering of flow cell components

Albeit often overlooked, the volume of the catholyte reservoir actually plays a crucial role in flow cell performance, as summarized in Fig. 5d. A small reservoir suffers rapid bicarbonate depletion during the electrochemical operations, which explains the expeditious FE decrease in the 30 mL reservoir compared with a 100 mL reservoir. Besides, the average production rates of formate at 200 mA/cm^2 and 300 mA/cm^2 are similar in a 30 mL reservoir, which indicates a limitation of the reactant supply. The FE of formate production for DRM-BiNS improved with the use of a larger reservoir, particularly at high current densities, highlighting the necessity of supplying adequate bicarbonate for sustained CO2RR performance.

Three typical catalyst loadings (0.5, 1, and 2 mg/cm^2) were employed for the DRM-BiNS catalyst at the same current density (both 100 and 200 mA/cm^2), but the observed FE remained essentially indifferent, except for the highest loading with the highest current density, as shown in Fig. S8a. The results strongly suggest the *i*-CO_2 is the limiting factor for the CO2RR performance.

Additionally, the effect of ionomer content on the flow cell performance was also studied by Lee et al. [34] They reported that excess ionomers could cover active sites, whereas insufficient ionomers result in catalyst detachment [34]. Three typical ionomer contents (5%, 10%, and 20%) were examined for the DRM-BiNS catalyst at an increased current density (both 300 and 400 mA/cm^2), and no significant change in FE was observed among the three ionomer contents across the two current densities (Figs. S8b and S9). Again, the insignificant influence of ionomer content further suggests the *i*-CO_2 is the limiting factor for cell performance.

Substrate selection plays a critical role in the performance of flow cells for CO_2 reduction reactions (CO_2RR). Typically, CO_2RR benefits from hydrophobic substrates, as they facilitate the formation of a well-defined three-phase interface, which enhances CO_2 availability at the catalyst surface. However, in the case of captured CO_2 reduction, dissolved CO_2 also plays a significant role, making hydrophilic substrates more favorable for improved CO_2 utilization. Given the need to balance these properties, Toray 060 (hydrophobic) and Freudenberg H23 (hydrophilic) were selected based on their thickness, structural characteristics, and hydrophilicity. As shown in Fig. S10, the Freudenberg H23 carbon paper exhibited superior performance compared to Toray 060 (79% vs. 67%), further highlighting the critical role of dissolved CO_2 in enhancing the efficiency of captured CO_2 reduction reactions.

Both CEM and BPM can serve as the functional membrane to provide a proton flux, which not only generates the needed *i*-CO_2 by reacting with bicarbonate but also conducts the ionic communication between the two electrodes. Although BPM is commonly considered to introduce higher resistance, leading to a higher operating potential (~0.8 V increase at 100 mA/cm^2), it also raises the anode pH from 1 (CEM) to 14 (BPM), reducing the potential by 0.767 V. As a result, the overall operating potential is very similar for both membranes. In this work, CEM and BPM were compared in terms of FE for an extended cell operation up to 180 min (Fig. S11). In the first hour, both CEM and BPM delivered a similarly high level of FE (83%–86%) at 100 mA/cm^2 with 100 mL catholyte; however, FE from the CEM-based cell quickly dropped from 86% at the 2nd 30-min to 54% at the 6th 30-min. By stark contrast, FE from the BPM-based cell was stable (84%–81%) during the entire testing period. In addition to proton cross-through the CEM, protons and potassium ions are inevitably exchanged through the CEM simultaneously due to the high concentration bias (high H^+ concentration in anolyte and high K^+ concentration in catholyte). As potassium ions accumulated in the anolyte and reached a certain concentration, the protons began to be partially replaced as charge carriers. Since potassium ions do not generate *i*-CO_2, it leads to a decline in formate FE during subsequent operation.

Both cation-conducting ionomers (such as Nafion) and anion-conducting ionomers (such as Sustainion) can be used as an electrochemical binder to immobilize a catalyst onto the electrode substrate. Fig. S12 compares the formate FE measured every 30 min over 3 h for electrodes using the two different ionomers. In the first hour of operation, both Nafion and Sustainion delivered high FE at the same level, around 83%–87%. However, the cation-conducting Nafion-coated electrode was not stable: FE dropped from 86% at the 2nd 30-min to 55% at the 6th 30-min. In contrast, the anion-conducting Sustainion maintained a stable FE throughout the test. Post-experiment SEM-EDX analysis of the electrode using Nafion revealed an O:K ratio close to 2:1, which can correspond to potassium formate (KCOOH). These results strongly suggest that the anion product is not efficiently transferred out of the catalyst layer when using the Nafion, leading to product accumulation on active catalyst sites to hurdle subsequent formate FE reduction. In comparison, the anion products can be effectively transported out by Sustainion, resulting in stable CO2RR performance.

3.4. Comparison of captured CO_2 reduction performance between DRM-Bi and OD-Bi

After all these optimizations in the cell design and operation conditions, the captured CO_2 reduction on DRM-BiNS exhibits a formate FE comparable to that of direct gas-fed CO_2 reduction, as illustrated in

Fig. S13. Gas products were also examined by GC, as shown in Fig. S14. Product distribution suggests that formate is the dominating product, along with a trace amount of CO (< 2% at 200 mA/cm^2). Fig. 6a compares the FE between DRM-BiNS and OD-Bi NS in a flow cell with a feedstock of either captured CO_2 or gas-fed CO_2. To elevate the performance difference, captured CO_2 reduction was performed in a flow cell with a 30 mL catholyte, representing a more CO_2-limiting environment. When reducing gas-phase CO_2, formate-oriented FE at 100 mA/cm^2 were comparable for DRM-BiNS and OD-BiNS (91% vs. 87%, respectively). However, at 200 mA/cm^2, DRM-BiNS exhibited approximately one-third higher FE to formate compared with OD-BiNS (85% vs. 67%). In the case of captured CO_2 reduction, the differences in FE to formate at 100 mA/cm^2 were less pronounced (81% for DRM-BiNS vs. 74% for OD-BiNS). At 200 mA/cm^2, however, DRM-BiNS demonstrated double the FE to formate relative to OD-BiNS (70% vs. 31%), highlighting its superior CO_2 reduction capability under CO_2-limited conditions. To prove this speculation, we tested double-loading OD-BiNS as a comparison. As shown in Fig. S15, at low current densities, the performance of the double-loading OD-BiNS closely matches that of DRM-BiNS, suggesting a comparable number of active sites, given that the intrinsic activity of both catalysts is similar. However, as the current increases, the double-loading OD-BiNS reaches a plateau, whereas DRM-BiNS continues to achieve higher current densities. This provides direct evidence that DRM-BiNS performs more effectively under CO_2-limited conditions (in H-cell condition and in 2.5 M $KHCO_3$ solution). To further evaluate its performance, flow cell tests for captured CO_2 reduction were conducted using an extended catholyte reservoir to ensure a consistent CO_2 supply, as shown in Fig. 6b. The two catalysts were tested under current densities ranging from 50 to 500 mA/cm^2. Under sufficient bicarbonate supply (200 mL catholyte), DRM-BiNS demonstrated a higher FE for formate production at high current densities, achieving over 80% FE at 200 mA/cm^2 and exceeding 50% FE at 500 mA/cm^2. At all current densities tested, DRM-BiNS demonstrated the superior FE to formate using OD-BiNS. At lower current densities, the FE difference between DRM-BiNS and OD-BiNS was about 10%–15%; however, at higher current densities, the FE difference between DRM-BiNS and OD-BiNS is more prominent: 20%–25% at 400–500 mA/cm^2, indicating a significantly enhanced CO2RR capability.

We used COMSOL to simulate the species at different current densities, as shown in Fig. S16. With the optimal catholyte channel thickness (300 μm) and the optimal flow rate (30 rpm or 3.63 cm/s of velocity), the impact of applied current density (from 100 to 500 mA/cm^2) was studied by simulation. As expected, increasing the applied current density brings higher H^+ concentration and higher $CO_{2,aq}$ concentration. However, the rate of increase is not identical for the two current densities: after 5 fold current density applied, 93% increase for H^+ concentration (1.29×10^{-8} to 2.49×10^{-8} M) vs. 88% increase for $CO_{2,aq}$ concentration (3.58 to 6.73 mM). Very interestingly, the maximum OH^- concentration also increases (from 1.04×10^{-6} M to 1.22×10^{-6} M, or 17% increase). Clearly, increasing current density will potentially lower both FE towards CO2RR and the activity of CO2RR because of both the rising H^+ concentration and slowing growth in $CO_{2,aq}$ concentration.

3.5. Durability

To evaluate the stability of the catalyst in a working cell, the flow cell was operated continuously for 20 h, with electrolyte replenishment every 5 h. The cell voltage, without any compensation, was stable in the entire 20-hour test, and the FE stood at the same level as shown in Fig. 7a. A comparison of the SEM and XRD results before and after the durability test reveals a negligible change in catalyst structure and species, demonstrating the superior stability for *i*-CO_2 to formate on DRM-BiNS (Fig. S17a, b, and c). In addition, the CV test exhibited negligible change in catalytic activity upon the 20-hour durability test (Fig. 7b), and the electrode capacitance showed insignificant change in surface area (Fig. 7c), which demonstrates a good stability of the catalyst. In comparison, OD-BiNS exhibited a significant decline in activity, with the FE dropping to ≤ 50% after approximately 6 h at 100 mA/cm^2, as shown in Fig. S18. This degradation is likely attributed to the absence of ligand protection [39].

As summarized in Table S2, our study demonstrates current densities

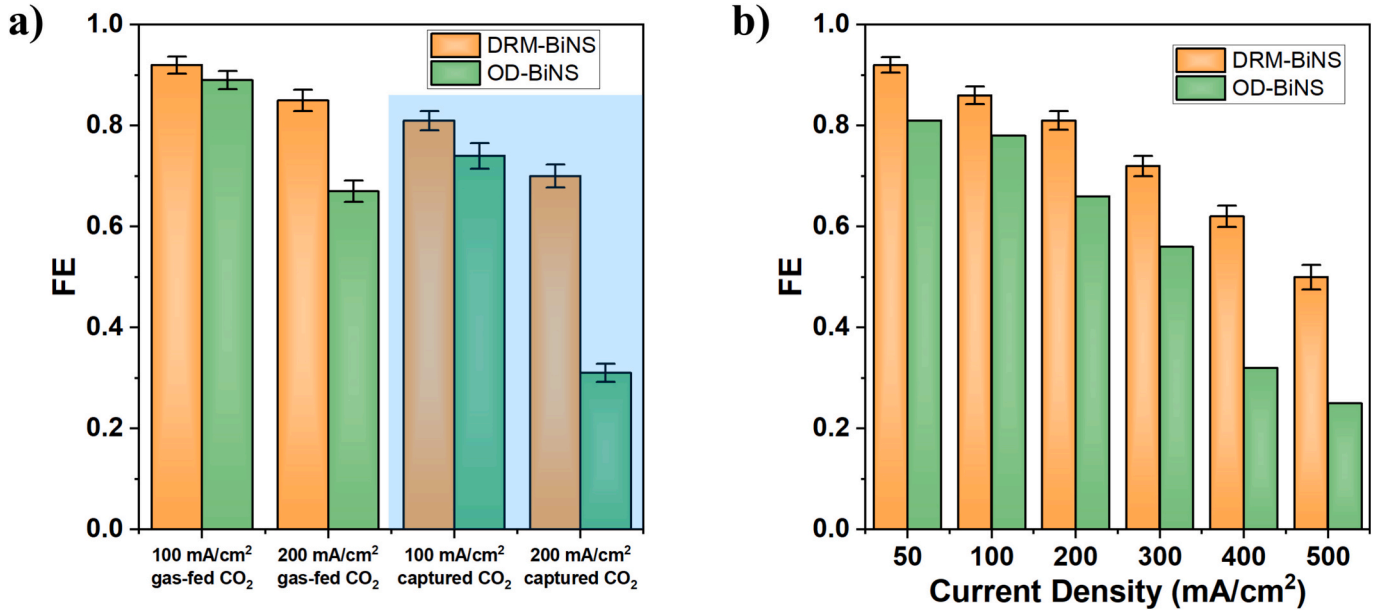

Fig. 6. Comparison between DRM-BiNS and OD-BiNS. (a) Cathode feedstock of either gas-fed CO_2 or captured CO_2 (30 mL of 2.5 M $KHCO_3$ solution) at two typical current densities (100 and 200 mA/cm^2). (b) Wide range of current density. (100 mL of 2.5 M $KHCO_3$ solution for 50–300 mA/cm^2; 200 mL of 2.5 M $KHCO_3$ solution for 400 and 500 mA/cm^2. Experiment conditions: Captured CO2RR: 30 rpm pump rate, 30 mL catholyte volume, horizontal orientation, 300 μm between membrane and cathode, 0.5 mg-Bi/cm^2 catalyst loading, 20% ionomer content, and H23 carbon paper as the substrate. Gas CO2RR: The experiment was conducted in a catholyte-free MEA flow cell. The anode was nickel foam, and the anolyte was 1 M KOH. The cathode was the DRM-BiNS normalized to 0.5 mg-Bi/cm^2 on Sigracet 39 BB carbon paper. The two electrodes were separated by an AEM (Sustainion X37–50 Grade RT).

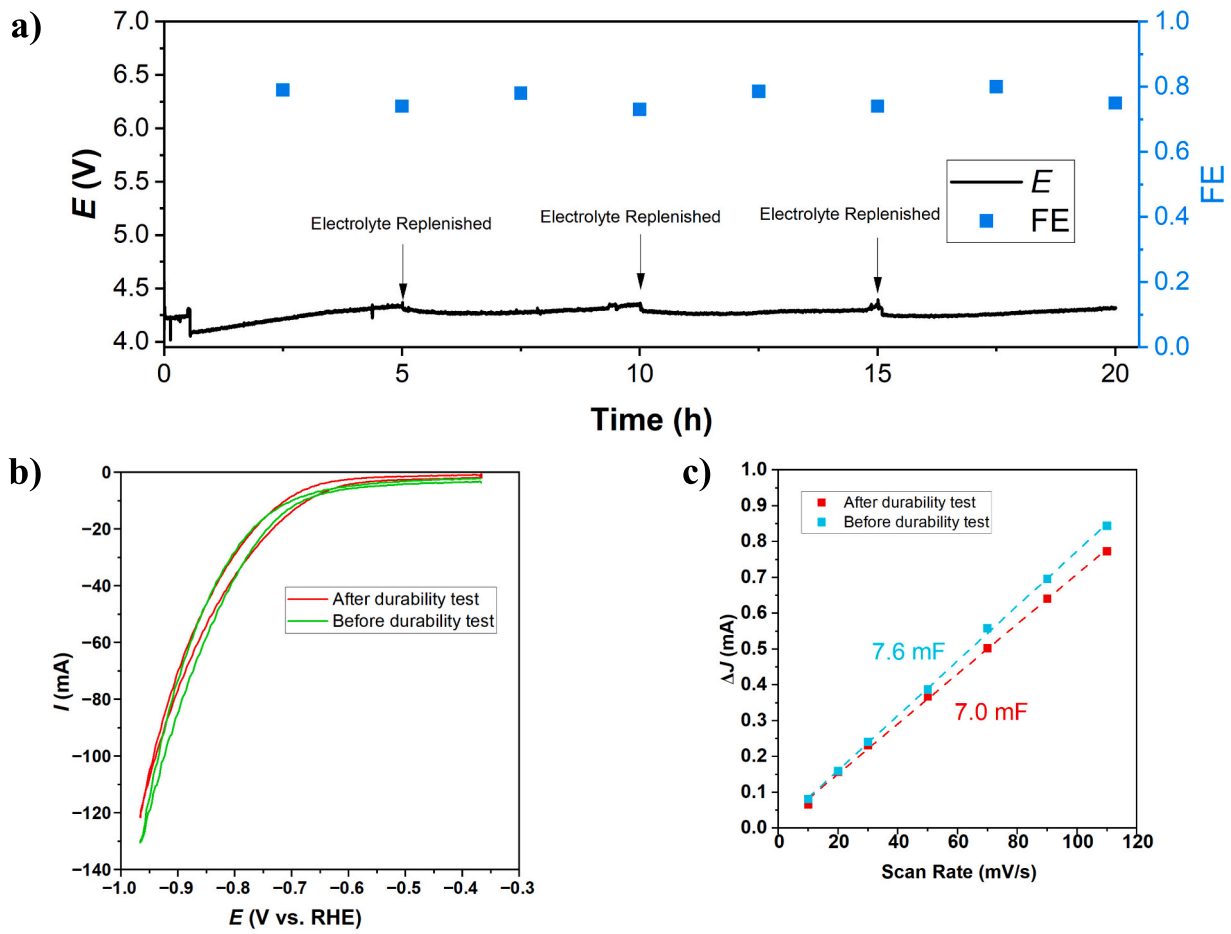

Fig. 7. Durability of DRM-BiNS-based CO2RR cell. (a) Potential profile and FE of the 20-hour durability test. (b) CV test before and after durability evaluation. (c) Electrode capacitance before and after durability test. Experiment conditions: 30 rpm pump rate, 1 L catholyte was replenished with fresh 2.5 M $KHCO_3$ solution every 5 h, horizontal orientation, 300 μm between membrane and cathode, 0.5 mg-Bi/cm^2 catalyst loading, 20% ionomer content, and H23 carbon paper as the substrate.

and FE for formate production that are comparable to those achieved in systems utilizing gaseous CO_2 as the reactant. Moreover, the current densities reported in this work significantly exceed those of previous studies employing captured CO_2 as a feedstock for formate production. These results underscore the exceptional performance of our catalyst and cell design in facilitating efficient captured CO_2 reduction.

4. Conclusion

In summary, DRM-BiNS with 2D nanosheet structure was successfully prepared as a new family of catalytic materials with large surface area and interconnected porosity for formate-producing CO2RR. By uniting experimentation and simulation, insights into structure-parameter-performance relation were acquired in flow cell setting, including critical membrane-electrode distance (300 μm), beneficial cell orientation (horizontal), and optimal peristaltic pumping rate (30 rpm). In addition, important cell components (such as catholyte volume, electrode substrate, membrane choice, and ionomer type) were also examined to enhance the CO2RR performance for DRM-BiNS catalytic system. By leveraging acquired structural/parametric insights, and engineered flow-cell components, and enabling DRM-BiNS catalysts, we achieved a formate-oriented FE comparable to that obtained with gas-phase CO_2 feedstock. In particular, the DRM-BiNS catalyst demonstrated an FE exceeding 80% at 200 mA/cm^2 and maintained an FE above 50% even at a current density of 500 mA/cm^2. This performance is significantly superior to that of previously reported OD-BiNS for captured CO_2 reduction. This study demonstrates the feasibility of integrating optimized flow cell configurations with advanced MOF-derived catalysts to achieve industrially relevant reaction rates and selectivity. The research outcome also highlights the potential of the synergistic study between experimentation and simulation for efficient captured CO_2 reduction in bicarbonate solutions at high current densities. The findings underscore the scalability and effectiveness of DRM-BiNS as a promising solution to address challenges in CO_2 conversion, paving the way for sustainable carbon utilization technologies.

CRediT authorship contribution statement

Tianlei Li: Methodology, Formal analysis, Writing – original draft, Investigation, Conceptualization. **Nabin Subedi:** Writing – review & editing, Data curation, Software. **Sujin Kang:** Investigation, Writing – review & editing, Data curation. **Qiqi Mao:** Methodology, Formal analysis, Writing – review & editing, Investigation. **Yuhuan Fei:** Investigation, Writing – review & editing. **Shuang Gu:** Writing – review & editing, Software, Funding acquisition, Supervision, Investigation. **Wenzhen Li:** Supervision, Investigation, Formal analysis, Writing – review & editing, Methodology, Funding acquisition, Conceptualization.

Declaration of competing interest

The authors declare that they have no known competing financial interests or personal relationships that could have appeared to influence the work reported in this paper.

Acknowledgements

This research of this work was supported by the U.S. NSF agency through both ECO-CBET program (2219162 & 2219172) and EPSCoR RII-Track-2 FEC program (2316481 & 2316482), and the U.S. DOE agency (DE-SC0025376). W.L. is grateful to his Herbert L. Stiles Professor fellowship. S.G. appreciates the Sam Bloomfield Chair Professor endowment. T.L. acknowledges the fruitful discussion with Mohammad Albloushi, Xiaopeng Liu, and Rod Alexei De Guzman. The authors also acknowledge Tracey P. Stewart for TEM analyses.

Appendix A. Supplementary data

Equations, additional structural characterization and supporting electrochemical characterization. Supplementary data to this article can be found online at https://doi.org/10.1016/j.cej.2025.165272.

Data availability

Data will be made available on request.

References

[1] U.S.E.P. Agency, Inventory of US Greenhouse Gas Emissions and Sinks: 1990–2019, 2024.
[2] J. Han, X. Bai, X. Xu, X. Bai, A. Husile, S. Zhang, L. Qi, J. Guan, Advances and challenges in the electrochemical reduction of carbon dioxide, Chem. Sci. 15 (2024) 7870–7907, https://doi.org/10.1039/D4SC01931H.
[3] C. Tang, Y. Zheng, M. Jaroniec, S.Z. Qiao, Electrocatalytic refinery for sustainable production of fuels and chemicals, Angew. Chem. Int. Ed. Engl. 60 (2021) 19572–19590, https://doi.org/10.1002/anie.202101522.
[4] M.G. Kibria, J.P. Edwards, C.M. Gabardo, C.-T. Dinh, A. Seifitokaldani, D. Sinton, E.H. Sargent, Electrochemical CO2 reduction into chemical feedstocks: from mechanistic electrocatalysis models to system design, Adv. Mater. 31 (2019) 1807166, https://doi.org/10.1002/adma.201807166.
[5] S. Vijay, W. Ju, S. Brückner, S.-C. Tsang, P. Strasser, K. Chan, Unified mechanistic understanding of CO2 reduction to CO on transition metal and single atom catalysts, Nature Catal. 4 (2021) 1024–1031, https://doi.org/10.1038/s41929-021-00705-y.
[6] C.-J. Chang, S.-C. Lin, H.-C. Chen, J. Wang, K.J. Zheng, Y. Zhu, H.M. Chen, Dynamic reoxidation/reduction-driven atomic interdiffusion for highly selective CO2 reduction toward methane, J. Am. Chem. Soc. 142 (2020) 12119–12132, https://doi.org/10.1021/jacs.0c01859.
[7] L. Li, A. Ozden, S. Guo, F.P. García de Arquer, C. Wang, M. Zhang, J. Zhang, H. Jiang, W. Wang, H. Dong, D. Sinton, E.H. Sargent, M. Zhong, Stable, active CO2 reduction to formate via redox-modulated stabilization of active sites, Nature Commun. 12 (2021) 5223, https://doi.org/10.1038/s41467-021-25573-9.
[8] H.S. Jeon, S. Kunze, F. Scholten, B. Roldan Cuenya, Prism-shaped Cu nanocatalysts for electrochemical CO2 reduction to ethylene, ACS Catal. 8 (2018) 531–535, https://doi.org/10.1021/acscatal.7b02959.
[9] H. Xu, D. Rebollar, H. He, L. Chong, Y. Liu, C. Liu, C.-J. Sun, T. Li, J.V. Muntean, R. E. Winans, D.-J. Liu, T. Xu, Highly selective electrocatalytic CO2 reduction to ethanol by metallic clusters dynamically formed from atomically dispersed copper, Nature Energy 5 (2020) 623–632, https://doi.org/10.1038/s41560-020-0666-x.
[10] J. Ding, H. Bin Yang, X.-L. Ma, S. Liu, W. Liu, Q. Mao, Y. Huang, J. Li, T. Zhang, B. Liu, A tin-based tandem electrocatalyst for CO2 reduction to ethanol with 80% selectivity, Nature Energy 8 (2023) 1386–1394, https://doi.org/10.1038/s41560-023-01389-3.
[11] C. Peng, G. Luo, J. Zhang, M. Chen, Z. Wang, T.-K. Sham, L. Zhang, Y. Li, G. Zheng, Double sulfur vacancies by lithium tuning enhance CO2 electroreduction to n-propanol, Nat. Commun. 12 (2021) 1580, https://doi.org/10.1038/s41467-021-21901-1.
[12] S.M. Jordaan, C. Wang, Electrocatalytic conversion of carbon dioxide for the Paris goals, Nature Catal. 4 (2021) 915–920, https://doi.org/10.1038/s41929-021-00704-z.
[13] M.R. Gruber, B. Hofko, M. Hoffmann, D. Stinglmayr, T.M. Seifried, H. Grothe, Deicing performance of common deicing agents for winter maintenance with and without corrosion-inhibiting substances, Cold Reg. Sci. Technol. 208 (2023) 103795, https://doi.org/10.1016/j.coldregions.2023.103795.
[14] S. Ha, R. Larsen, Y. Zhu, R.I. Masel, Direct formic acid fuel cells with 600 mA cm–2 at 0.4 V and 22 °C, Fuel Cells 4 (2004) 337–343, https://doi.org/10.1002/fuce.200400052.
[15] C. Guo, W. Zhou, X. Lan, Y. Wang, T. Li, S. Han, Y. Yu, B. Zhang, Electrochemical upgrading of formic acid to formamide via coupling nitrite co-reduction, J. Am. Chem. Soc. 144 (2022) 16006–16011, https://doi.org/10.1021/jacs.2c05660.
[16] I. Grigioni, L.K. Sagar, Y.C. Li, G. Lee, Y. Yan, K. Bertens, R.K. Miao, X. Wang, J. Abed, D.H. Won, F.P. García de Arquer, A.H. Ip, D. Sinton, E.H. Sargent, CO2 electroreduction to formate at a partial current density of 930 mA cm–2 with InP colloidal quantum dot derived catalysts, ACS Energy Lett. 6 (2021) 79–84, https://doi.org/10.1021/acsenergylett.0c02165.
[17] S. Zhang, P. Kang, T.J. Meyer, Nanostructured tin catalysts for selective electrochemical reduction of carbon dioxide to formate, J. Am. Chem. Soc. 136 (2014) 1734–1737, https://doi.org/10.1021/ja4113885.
[18] W. Yang, C. Si, Y. Zhao, Q. Wei, G. Jia, G. Cheng, J. Qin, Z. Zhang, Activating inert antimony for selective CO2 electroreduction to formate via bimetallic interactions, Appl. Catal. Environ. 316 (2022) 121619, https://doi.org/10.1016/j.apcatb.2022.121619.
[19] W. Ma, S. Xie, X.-G. Zhang, F. Sun, J. Kang, Z. Jiang, Q. Zhang, D.-Y. Wu, Y. Wang, Promoting electrocatalytic CO2 reduction to formate via sulfur-boosting water activation on indium surfaces, Nat. Commun. 10 (2019) 892, https://doi.org/10.1038/s41467-019-08805-x.
[20] H. Zheng, G. Wu, G. Gao, X. Wang, The bismuth architecture assembled by nanotubes used as highly efficient electrocatalyst for CO2 reduction to formate, Chem. Eng. J. 421 (2021) 129606, https://doi.org/10.1016/j.cej.2021.129606.
[21] E. Deady, C. Moon, K. Moore, K.M. Goodenough, R.K. Shail, Bismuth: economic geology and value chains, Ore Geol. Rev. 143 (2022) 104722. https://www.sciencedirect.com/science/article/pii/S0169136822000300.
[22] Y. Xing, X. Kong, X. Guo, Y. Liu, Q. Li, Y. Zhang, Y. Sheng, X. Yang, Z. Geng, J. Zeng, Bi@Sn core–shell structure with compressive strain boosts the electroreduction of co2 into formic acid, Adv. Sci. 7 (2020), https://doi.org/10.1002/advs.201902989.
[23] Q. Gong, P. Ding, M. Xu, X. Zhu, M. Wang, J. Deng, Q. Ma, N. Han, Y. Zhu, J. Lu, Z. Feng, Y. Li, W. Zhou, Y. Li, Structural defects on converted bismuth oxide nanotubes enable highly active electrocatalysis of carbon dioxide reduction, Nat. Commun. 10 (2019), https://doi.org/10.1038/s41467-019-10819-4.
[24] J. Yang, X. Wang, Y. Qu, X. Wang, H. Huo, Q. Fan, J. Wang, L.M. Yang, Y. Wu, Bi-based metal-organic framework derived leafy bismuth nanosheets for carbon dioxide electroreduction, Adv. Energy Mater. 10 (2020). https://www.scopus.com/inward/record.uri?eid=2-s2.0-85088816907&doi=10.1002%2faenm.202001709&partnerID=40&md5=77df641c181516525997a0c8bc6f9d3e.
[25] N. Han, Y. Wang, H. Yang, J. Deng, J. Wu, Y. Li, Y. Li, Ultrathin bismuth nanosheets from in situ topotactic transformation for selective electrocatalytic CO2 reduction to formate, Nat. Commun. 9 (2018) 1320, https://doi.org/10.1038/s41467-018-03712-z.
[26] K. Fan, Y. Jia, Y. Ji, P. Kuang, B. Zhu, X. Liu, J. Yu, Curved surface boosts electrochemical CO2 reduction to formate via bismuth nanotubes in a wide potential window, ACS Catal. 10 (2020) 358–364, https://doi.org/10.1021/acscatal.9b04516.
[27] Z.B. Hoffman, T.S. Gray, Y. Xu, Q. Lin, T.B. Gunnoe, G. Zangari, High selectivity towards formate production by electrochemical reduction of carbon dioxide at copper–bismuth dendrites, ChemSusChem 12 (2019) 231–239, https://doi.org/10.1002/cssc.201801708.
[28] L. Liu, K. Yao, J. Fu, Y. Huang, N. Li, H. Liang, Bismuth metal-organic framework for electroreduction of carbon dioxide, Colloids Surf. A Physicochem. Eng. Asp. 633 (2022) 127840. https://www.sciencedirect.com/science/article/pii/S092777572101709X.
[29] J.B. Greenblatt, D.J. Miller, J.W. Ager, F.A. Houle, I.D. Sharp, The technical and energetic challenges of separating (photo)electrochemical carbon dioxide reduction products, Joule 2 (2018) 381–420, https://doi.org/10.1016/j.joule.2018.01.014.
[30] D.W. Keith, G. Holmes, D. St, K. Heidel Angelo, A process for capturing CO2 from the atmosphere, Joule 2 (2018) 1573–1594, https://doi.org/10.1016/j.joule.2018.05.006.
[31] F. Sabatino, M. Mehta, A. Grimm, M. Gazzani, F. Gallucci, G.J. Kramer, M. van Sint Annaland, Evaluation of a direct air capture process combining wet scrubbing and bipolar membrane electrodialysis, Ind. Eng. Chem. Res. 59 (2020) 7007–7020, https://doi.org/10.1021/acs.iecr.9b05641.
[32] X. Zhang, Y. Zhang, Q. Li, X. Zhou, Q. Li, J. Yi, Y. Liu, J. Zhang, Highly efficient and durable aqueous electrocatalytic reduction of CO2 to HCOOH with a novel bismuth–MOF: experimental and DFT studies, J. Mater. Chem. A 8 (2020) 9776–9787, https://doi.org/10.1039/D0TA00384K.
[33] D.M. Weekes, D.A. Salvatore, A. Reyes, A. Huang, C.P. Berlinguette, Electrolytic CO2 reduction in a flow cell, Acc. Chem. Res. 51 (2018) 910–918, https://doi.org/10.1021/acs.accounts.8b00010.
[34] E.W. Lees, M. Goldman, A.G. Fink, D.J. Dvorak, D.A. Salvatore, Z. Zhang, N.W. X. Loo, C.P. Berlinguette, Electrodes designed for converting bicarbonate into CO, ACS Energy Lett. 5 (2020) 2165–2173, https://doi.org/10.1021/acsenergylett.0c00898.
[35] J. Lee, H. Liu, Y. Chen, W. Li, Bismuth nanosheets derived by in situ morphology transformation of bismuth oxides for selective electrochemical CO2 reduction to formate, ACS Appl. Mater. Interfaces 14 (2022) 14210–14217, https://doi.org/10.1021/acsami.1c25217.
[36] Y.-X. Duan, Y.-T. Zhou, Z. Yu, D.-X. Liu, Z. Wen, J.-M. Yan, Q. Jiang, Boosting production of HCOOH from CO2 electroreduction via Bi/CeO, Angew. Chem. Int. Ed. 60 (2021) 8798–8802, https://doi.org/10.1002/anie.202015713.
[37] P. Deng, H. Wang, R. Qi, J. Zhu, S. Chen, F. Yang, L. Zhou, K. Qi, H. Liu, B.Y. Xia, Bismuth oxides with enhanced bismuth–oxygen structure for efficient

electrochemical reduction of carbon dioxide to formate, ACS Catal. 10 (2020) 743–750, https://doi.org/10.1021/acscatal.9b04043.
[38] G. Lee, A.S. Rasouli, B.-H. Lee, J. Zhang, D.H. Won, Y.C. Xiao, J.P. Edwards, M. G. Lee, E.D. Jung, F. Arabyarmohammadi, H. Liu, I. Grigioni, J. Abed, T. Alkayyali, S. Liu, K. Xie, R.K. Miao, S. Park, R. Dorakhan, Y. Zhao, C.P. O'Brien, Z. Chen, D. Sinton, E. Sargent, CO₂ electroreduction to multicarbon products from carbonate capture liquid, Joule 7 (2023) 1277–1288, https://doi.org/10.1016/j.joule.2023.05.003.
[39] N. Li, P. Yan, Y. Tang, J. Wang, X.-Y. Yu, H.B. Wu, In-situ formation of ligand-stabilized bismuth nanosheets for efficient CO2 conversion, Appl. Catal. Environ. 297 (2021) 120481, https://doi.org/10.1016/j.apcatb.2021.120481.